

Advanced Characterisation of Pore Structure in Next-Generation Reactor Graphites

Bradley Moresby-White^a, Katie L. Jones^{a,*}, G. Peter Matthews^a, Giuliano M. Laudone^a

^aFaculty of Science and Engineering, University of Plymouth, Plymouth, UK

Abstract

Nuclear grade graphite

Keywords: keyword, keyword, keyword

1. Introduction

2. Methodology

2.1. Materials

Virgin graphite samples of two grades, IG110 and IG430, were supplied by Toyo Tanso LtdTM, Osaka, Japan. The properties of both grades are tabulated (Table 1). IG-110 is currently employed in the three existing HTGRs worldwide, while IG-430 is designed to deliver increased density, strength, and thermal conductivity for future applications.[1] (Table 1). Both grades comply with ASTMD7219-19, including the requirement for a minimum bulk density exceeding 1.7 g/cm³ [2] (Table 1).

2.2. Sample preparation

Cuboids were sub-sampled from the virgin graphite blocks, with dimensions of approximately 10mm x 10mm x 100mm. The sub-samples were further subsampled into cuboids of side lengths 7mm, providing 3 cuboids per grade. Samples were polished via SiC polishing pads up to a grit size of P5000, to minimise topographical variations induced by sample preparation that may cause artefacts during SEM imaging or low pressure gas adsorption [4, 3]. Samples were sonicated in 2-propanol for 24h to remove any contaminants, particularly the lubricant used in the machining process. Samples were then dried under vacuum for 12

h at 305 ± 5 °C using the BELPREP-vac (MicrotracBEL, Japan) in order to remove any residual moisture introduced during the sonication process.

2.3. Micrograph generation

The JEOLTMIT510 Scanning Electron Microscope was used in the generation of the contiguous set of individual micrographs from which the full composite micrograph is assembled. The *Image Montage* capability, within the JEOLInScopeTM package, performed this function. The system captures a number of micrographs, with the motorised stage moving the electron beam over the specified area with a set overlap to capture each new micrograph, with the software adjusting stigmation, contrast, and brightness. Shifts in contrast and brightness were on the order of < 1% and thus negligible in affecting intensity threshold for the full composite. The full set of parameters selected are tabulated (Table 2).

2.4. Composite assembly

The composite assembly (i.e., "stitching") stage, where the overlapping micrographs are assembled into a single image per sample, may have a significant impact on the porosity values generated as incorrect fusion will misrepresent pore structures. A stitching method based on the phase correlation approach originally developed by Kuglin and Hines, amongst the most popular approaches to image registration, was selected and operated as a plug-in within ImageJ [5, 6]. This method represents a development of the original phase correlation method[6].

Is this necessary?
I do like it, talking about the standards, but it is a bit of a tangent.

for the following table, better to directly cite the manuf?

Could talk here about how we wanted to do resin impeg like Kane et al, but did not have the chance, and explain this might introduce issues

Make sure to double check that figure for ACB

*Corresponding author.

Email address: katie.jones@plymouth.ac.uk (Katie L. Jones)

Table 1: Manufacturer dataset for IG-110 and IG-430 [3]

Grade	Coke source	Bulk density/g cm ³	Filler particle size/ μm	Tensile strength/MPa	Young's modulus/GPa	Thermal conductivity/W m ⁻¹ K ⁻¹
IG-110	Petrol 1	1.77	10	25	9.8	120
IG-430	Pitch	1.82	10	37	10.8	140

Table 2: Parameters for composite assembly captured with the JEOL IT510 SEM using Image Montage Mode

Parameters	Values
Magnification (\times)	1000
Resolution ($\mu\text{m}/\text{px}$)	0.1
Surface area per micrograph (μm^2)	12 288
Overlap (%)	10
Micrographs per sample (n)	196

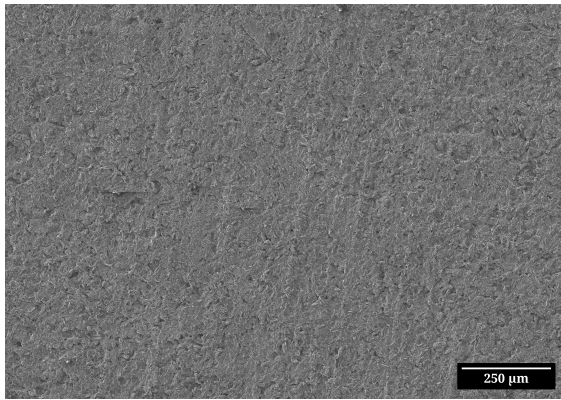


Figure 1: Fully assembled SEM composite: IG-430 Sample C, 1000 \times magnification, 5 kV accelerating voltage. Bar = 250 μm .

A key advantage of this method is the avoidance of error propagation by consecutive registration steps, which is key at this scale [6]. A further advantage is the sub-pixel accuracy of the fusion, as incorrect alignments would generate false pore diameters. The resulting composite micrographs showed excellent alignment with no visible delineation between individual micrographs, a total area comparable with previous works, high resolution, and clear distinction between porosity and bulk when examined closely (Figure 1 [7, 8]).

2.5. Computation of Channel Porosity

2.5.1. Intensity/Greyscale Thresholding

Intensity thresholding determines a greyscale value at which porosity and bulk (i.e., foreground and background) are distinguished. This requires the representation of the frequency of greyscale values for each of the pixels in the micrograph into a

histogram of intensity, enabling the selection of an image-wide threshold at which different classes can be separated.

For each 8-bit micrograph E (pixel values $0 \leq E(x, y) \leq 255$), we first compute its intensity histogram $H(i)$ for $i = 0, 1, \dots, 255$. Specifically,

$$H(i) = \sum_{x=1}^M \sum_{y=1}^N \mathbf{1}\{E(x, y) = i\},$$

where M and N are the image width and height (in pixels), and

$$\mathbf{1}\{E(x, y) = i\} = \begin{cases} 1, & \text{if the pixel at } (x, y) \text{ has intensity } i, \\ 0, & \text{otherwise.} \end{cases}$$

In essence, for each pixel the equation checks the greyscale value and increments the count in the corresponding bin, yielding a 256-bin histogram $H(i)$ whose entries count the number of pixels at each greyscale level.

Global automatic thresholding algorithms optimise by different criteria (i.e. maximisation of inter-class variance, minimisation of intra-class variance) to determine thresholds. For manual selection of a given threshold, or validation of an automatically selected threshold, there exists no certain criteria to allow a fully objective evaluation [7]. Thresholding aims to select an intensity value that reliably binarizes porosity and bulk in a way that minimizes both Type I and II errors, as evaluated by the operator (i.e., false positives, classifying a pore where one is not present, and false negatives, not classifying a pore where one is present).

A test of all 17 of the available automatic thresholding methods available in ImageJ demonstrated that none of the available automatic global intensity thresholding algorithm effectively distinguished between porosity and bulk with the sensitivity required to allow the classification of pores for the given histogram (Figure 3). The key cause is likely the lack of a bimodal distribution in the histograms generated by any of the micrographs, meaning that there are statistically no classes to be separated (Figure 2).

A HITL (human in the loop) approach was therefore undertaken, as illustrated in the process dia-

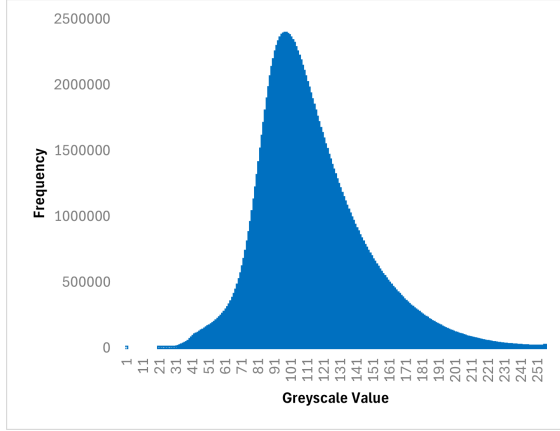


Figure 2: PLACEDHOLDER DRAFT: Histogram of greyscale values for IG-430 Sample F, 1000 \times , Showing skewness and unimodality

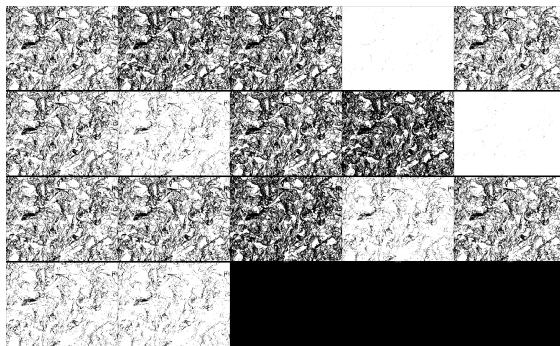


Figure 3: Thresholded Micrograph of IG-430 Sample C at 1000 \times Magnification. Methods are labelled sequentially from right to left, row by row. (a) Default (b) Huang (c) Huang2 (d) Intermodes (e) IsoData (f) Li (g) MaxEntropy (h) Mean (i) MinError(I) (j) Minimum (k) Moments (l) Otsu (m) Percentile (n) RenyiEntropy (o) Shanbhag (p) Triangle (q) Yen

gram (Figure 4). Here, the operator subsamples the overall fused composite, then examines this subsample to determine the threshold at which porosity and bulk are best separated. The operator then applies this threshold, along with a pore diameter threshold, to the full composite. The results are classified as either porosity or bulk to derive channel porosity.

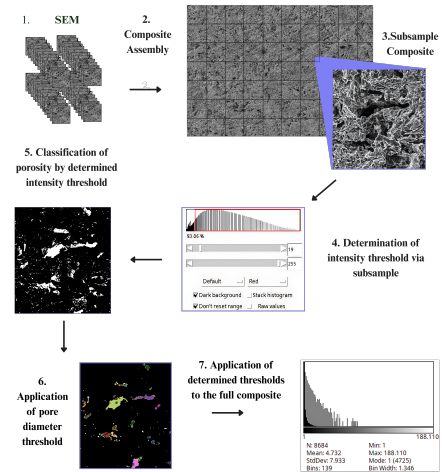


Figure 4: Full thresholding workflow detailing the process of micrograph generation, composite assembly, subsampling, intensity thresholding, and pore diameter thresholding.

2.5.2. Pore Diameter Thresholding

Pore size thresholds were imposed in this work, following previous studies [9, 7, 8], to restrict the automated recognition of pores to a range (i.e., only counting pores $> 12.5\mu\text{m}^2$) where classification is deemed reliable. However, this approach is inherently limited by the practical difficulty of objectively determining whether any given pore classification is correct.

As shown in (Table 3), extreme changes in the total pore count result from minor alterations in the threshold, with a $0.5\mu\text{m}^2$ threshold yielding a total pore count of 11,375, while a $1\mu\text{m}^2$ threshold yields a pore count of 6,485. Crucially however the total area of pores above the threshold remains relatively stable, with a porosity of 3.8% for the $0.5\mu\text{m}^2$ threshold, and 3.6% for the $1\mu\text{m}^2$ threshold. When combined with individual analyses of the resulting PSDs and precise examination of exactly which features are excluded at each threshold as per

Table 3: Effect of different pore area thresholds on IG-430F, showing the resulting pore count, total area, average pore size, and percentage area.

Area Threshold (μm^2)	0	0.5	1	2	4	8
Count	254261	11375	6485	4085	2812	1881
Total Area (μm^2)	71219	56722	53361	50063.63	46518	41161
Avg. Size (μm^2)	0.28	4.987	8.229	12.255	16.543	21.883
% Area	4.786	3.812	3.586	3.364	3.126	2.766

(Figure 5), it is clear that a pore area threshold of $1 \mu\text{m}^2$ ($\text{dia} = 1.12 \mu\text{m}$) was the optimal compromise between type I and II errors.

Crucially, setting such a threshold does not imply that no pores exist below this limit. Rather, it acknowledges that the confidence in classifying pores below the threshold is too low for reliable use. In this work, the limitations of any single technique are compensated by the strengths of others. During modelling, we select an interval over which the channel porosity determined from SEM imaging can reliably constrain the outputs of the inverse modelling process. Thus, no type II errors are introduced in the final model due to pore size thresholding, thanks to the combined use of alternative techniques and the ability to specify an interval within PoreXpert v.3.

2.5.3. Channel Porosity Analysis and Calculation

Following the determination of the above thresholds, the channel porosity was calculated using the “Analyse Particles” function in ImageJ. This function scans the micrograph pixel by pixel, identifies all pixels that surpass the intensity threshold, and groups them into connected regions via a flood-fill algorithm. Connectivity is defined based on the 8-connected (Moore neighborhood) criterion, whereby a pixel at (x, y) is considered connected to its eight immediate neighbors:

$$(x-1, y-1), (x-1, y), (x-1, y+1), (x, y-1), \\ (x, y+1), (x+1, y-1), (x+1, y), (x+1, y+1)$$

Thus, any two pixels that exceed the intensity threshold and are either directly adjacent or diagonally connected are classified as belonging to the same region (pore). The function then computes the area of each pore by converting the pixel count into physical area (i.e., 10 pixels per micrometre). Regions that do not meet the area threshold are omitted. The final results are a pore size distribution (PSD) and the channel porosity (%).

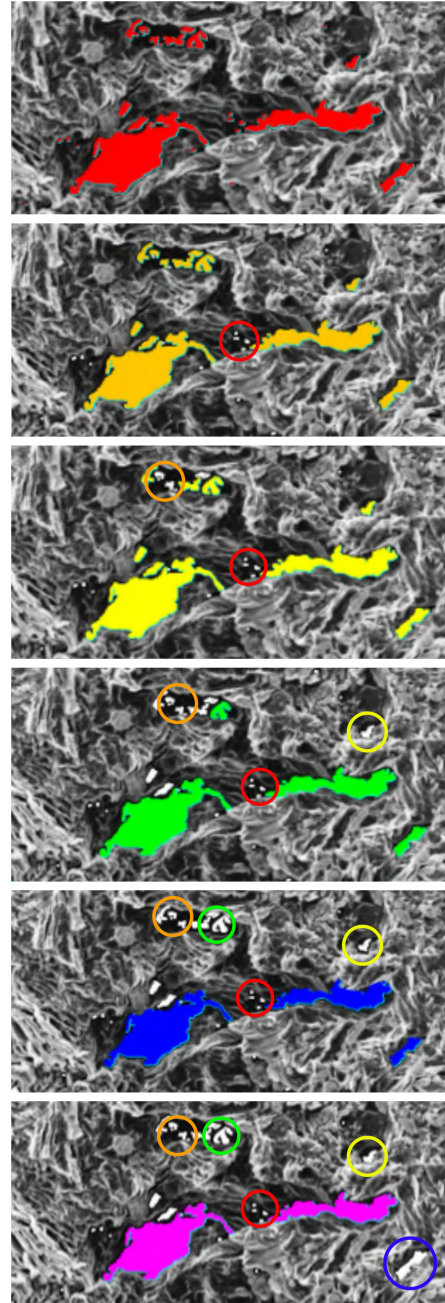


Figure 5: Effect of minimum area threshold on pore identification in subsample of IG-110 Sample B. Highlighted circles denote features which surpassed the previous threshold(s) only, indicated by colour. Thresholds applied (a-f, left-to-right, top-to-bottom): None, $0.5 \mu\text{m}^2$, $1 \mu\text{m}^2$, $2 \mu\text{m}^2$, $4 \mu\text{m}^2$, and $8 \mu\text{m}^2$.

insert theoretical density here

2.6. Helium (He) Pycnometry

Skeletal density was obtained using a Pycnomatic ATC pycnometer (Thermo Fisher Scientific, Italy) at a temperature of $20.00 \pm 0.01^\circ\text{C}$. Measurements were taken in ten replicates per sample, calculating the arithmetic mean.

Solid phase volume V_{SOLID} was calculated assuming a theoretical density of g cm^{-3} for an ideal graphite crystal. Closed Pore Volume (CPV) and Open Pore Volume (OPV) for each of the samples was calculated via equations 1 and 2.

$$\text{CPV} = \frac{m - V_{\text{SOLID}} \times \rho_s}{\rho_s} \quad (1)$$

$$\text{OPV} = V_{\text{BULK}} - \text{CPV} - V_{\text{SOLID}} \quad (2)$$

Specific Pore Volume (SPV), the void volume accessible to helium per gram of sample was calculated via Equation 3.

$$\text{SPV} = \frac{1}{\rho} - \frac{1}{\rho_s} \quad (3)$$

2.7. Mercury (Hg) Intrusion Porosimetry

Mercury intrusion porosimetry operates on the fundamental principle that the pressure at which a non-wetting fluid intrudes a given pore is inversely proportional to the diameter of that pore (i.e., the larger the pore, the easier it is for the non-wetting fluid to enter it). The exact physical relationship between diameter and applied pressure is governed by the Laplace Equation (Eq. 4)

$$d = \frac{-4\gamma \cos \theta}{P} \quad (4)$$

The pore diameter d is calculated using the equation:

- d (m): Pore diameter
- γ (N/m): Surface tension of the fluid
- θ (degrees): Contact angle of the fluid with the surface
- P_{app} (P): Pressure

Values of 140° and 130° were used for advancing and receding contact angles respectively, while a value of 0.480 N m^{-1} was assumed for the surface tension of mercury [10].

In this work, the dataset generated by Jones et al. [3] was used, representing measurements performed

not only on the same grades of graphite, but the same batch of graphites (i.e. sampled from the same larger "brick") as those samples which underwent SEM imaging and He pycnometry in this work.

2.8. Nitrogen (N_2) Adsorption

Low-pressure gas adsorption isotherms were obtained using a BELSORP-max volumetric gas adsorption instrument (MicrotracBEL, Japan).

As with mercury intrusion porosimetry, the dataset generated by Jones et al. [3] was used in this work. Once more, this represents measurements performed on the same grades but the same batch of graphites (i.e. sampled from the same larger "brick") as those samples which underwent SEM imaging and He pycnometry in this work.

3. Modelling

Hg intrusion porosimetry cannot capture the full range of pore sizes. Hence, the use of GCMC to "stitch" together the pore diameter ranges covered by both Hg and He adsorption [3]. The pore size distribution (PSD) is generated by combining the methods into a single set of values, which PoreXpert inversely models to capture.

References

- [1] Toyo Tanso Co., Ltd., Atomic power and nuclear fusion, accessed April 21, 2025 (2025). URL <https://www.toyotanso.com/us/en/Products/application/atomic-nuclear.html>
- [2] ASTM International, D7219-19 Standard Specification for Isotropic and Near-isotropic Nuclear Graphites, published August 2019; supersedes D7219-08R14 (2019).
- [3] K. Jones, G. Laudone, G. Matthews, A multi-technique experimental and modelling study of the porous structure of ig-110 and ig-430 nuclear graphite, *Carbon* 128 (2018) 1–11. doi:10.1016/j.carbon.2017.11.076.
- [4] N. Fang, R. Birch, T. Britton, Optimizing broad ion beam polishing of zircaloy-4 for electron backscatter diffraction analysis, *Micron* 159 (2022) 103268. doi:10.1016/j.micron.2022.103268.
- [5] C. Kuglin, D. Hines, The phase correlation image alignment method, in: Proceedings of the International Conference on Cybernetics and Society, 1975, pp. 163–165.
- [6] S. Preibisch, S. Saalfeld, P. Tomancak, Globally optimal stitching of tiled 3d microscopic image acquisitions, *Bioinformatics* 25 (11) (2009) 1463–1465. arXiv:2009 Apr 3, doi:10.1093/bioinformatics/btp184.
- [7] Q. Huang, H. Tang, Porosity analysis of superfine-grain graphite ig-110 and ultrafine-grain graphite t220, *Materials Science and Technology* 35 (8) (2019) 962–968. doi:10.1080/02670836.2019.1599557.
- [8] J. Kane, et al., Microstructural characterization and pore structure analysis of nuclear graphite, *Journal of Nuclear Materials* 415 (2) (2011) 189–197. doi:10.1016/j.jnucmat.2011.05.053.
- [9] J. Taylor, G. Hall, P. Mummery, Investigating the effects of stress on the pore structures of nuclear grade graphites, *Journal of Nuclear Materials* 470 (2016) 216–228. doi:10.1016/j.jnucmat.2015.12.031.
- [10] J. Van Brakel, S. Modrý, M. Svatá, Mercury porosimetry: state of the art, *Powder Technology* 29 (1) (1981) 1–12. doi:[https://doi.org/10.1016/0032-5910\(81\)85001-2](https://doi.org/10.1016/0032-5910(81)85001-2). URL <https://www.sciencedirect.com/science/article/pii/0032591081850012>